Materials Today Advances 21 (2024) 100467

Contents lists available at ScienceDirect

Materials Today Advances

journal homepage: www.journals.elsevier.com/materials-today-advances/

Green growth of mixed valence manganese oxides on quasi-freestanding bilayer epitaxial graphene-silicon carbide substrates

Michael Pedowitz [a,b,*], Daniel Lewis [a,b], Jennifer DeMell [a,b,c], Daniel J. Pennachio [d], Jenifer R. Hajzus [d], Rachael Myers-Ward [d], Soaram Kim [a,b,e,f], Kevin M. Daniels [a,b,**]

[a] *Department of Electrical and Computer Engineering, University of Maryland, College Park, MD, USA*
[b] *Institute for Research in Electronics and Applied Physics, University of Maryland, College Park, MD, USA*
[c] *Laboratory for Physical Sciences, College Park, MD, USA*
[d] *US Naval Research Laboratory, Washington DC, USA*
[e] *Department of Electrical and Computer Engineering, Texas A&M University, College Station, TX, USA 77843*
[f] *Center for Remote Health Technologies and Systems, Texas A&M University, College Station, TX, USA 77843*

ARTICLE INFO

Keywords:
Electrodeposition
Graphene
Epitaxial transition metal oxides
δ-MnO_2
Transformation
Low defect

ABSTRACT

Nanostructured manganese oxides (MnO_x) have shown incredible promise in constructing next-generation energy storage and catalytic systems. However, it has proven challenging to integrate with other low-dimensional materials due to harsh deposition conditions and poor structural stability. Here, we report the deposition of layered manganese dioxide (δ-MnO_2) on bilayer epitaxial graphene (QEG) using a simple three-step electrochemical process involving no harsh chemicals. Using this process we can synthesize a 50 nm thick H–MnO_2 film in 1.25s. This synthetic birnessite is inherently water-stabilized, the first reported in the literature. We also confirm that this process does not cause structural damage to the QEG, as evidenced by the lack of D peak formation. This QEG heterostructure enhanced MnO_2's redox active gas sensing, enabling room temperature detection of NH_3 and NO_2. We also report on transforming this δ-MnO_2 to other MnO_x compounds, Mn_2O_3 and Mn_3O_4, via mild annealing. This is confirmed by Raman spectroscopy of the films, which also confirms limited damage to the QEG substrate. To our knowledge, this is the first synthesis of Mn_2O_3 and Mn_3O_4 on pristine graphene substrates. Both methods demonstrate the potential of depositing and transforming multifunctional oxides on single-crystal graphene using QEG substrates, allowing for the formation of nanostructured heterostructures previously unseen. Additionally, the electrochemical nature of the deposition presents the ability to scale the process to the QEG wafer and adjust the solution to produce other powerful multifunctional oxides.

1. Introduction

The successful synthesis of graphene, a 2-dimensional layer of sp^2-hybridization carbon atoms, demonstrated the viability and enhanced properties of nano and nanostructured materials [1]. Since this discovery, nanomaterials and the interaction of these materials with traditional functional materials have been the subject of great excitement in the literature. Of the traditional materials paired with graphene, multivalent transition metal oxides (TMOs) have seen significant interest due to their strong redox capabilities, enabling their use in catalysis [2], next-generation energy storage [3], and gas sensing [4] applications.

Of the multivalent TMOs, manganese oxides (MnO_x) have attracted significant interest due to their environmental availability [5], low toxicity [5], and a large number of stable oxygen stoichiometries (MnO_2, Mn_2O_3, Mn_3O_4, and MnO) [6]. These MnO_x materials have been successfully utilized in catalysis [7], gas sensing [8], and energy storage [9–11] and have demonstrated novel magnetic properties in the low dimensional limit [12]. In catalysis, these MnO_x structures are comparable to noble metal catalysts, e.g., $T_{100} = 240\ ^\circ C$ for toluene reduction vs. $T_{100} = 230\ ^\circ C$ for platinum-based catalytic systems [7,13]. In energy storage MnO_x, materials are a primary contender for cathodes in next-generation multivalent battery systems (Zn/Zn^{+2}, Al/Al^{+3}) [9,10]. However, the use of MnO_x materials is hampered by their low electrical

---

* Corresponding author. Department of Electrical and Computer Engineering, University of Maryland, College Park, MD, USA

** Corresponding author. Department of Electrical and Computer Engineering, University of Maryland, College Park, MD, USA

E-mail addresses: mpedowit@umd.edu (M. Pedowitz), danielkm@umd.edu (K.M. Daniels).

https://doi.org/10.1016/j.mtadv.2024.100467
Received 10 October 2023; Received in revised form 19 January 2024; Accepted 19 January 2024

conductivity (10^{-5}-10^{-6} S) [14,15], which significantly reduces the speed of the surface redox reactions used to drive catalysis and energy storage. To counter this, heterostructures have been formed between manganese oxides and graphene, which seek to couple the high electrical conductivity of graphene with the redox activity of MnOx compounds [4].

A wide variety of methods have been demonstrated to produce these heterostructures. MnO_2/graphene heterostructures have been the most extensively synthesized by hydrothermal [16], solvothermal [17], microwave-assisted [18], and co-precipitation [19] methods. Alternate manganese oxides have seen less synthesis, but Mn_2O_3 and Mn_3O_4 graphene heterostructures have been produced via reflux [20] and co-precipitation methods [21], respectively. These methods, however, rely on modified Hummer's methods to produce MnO_x-graphene heterostructures. Modified Hummer's methods produce graphene oxide and reduced graphene oxide via the reaction of permanganate salts (e.g., $KMnO_4$) with graphite [16]. This significantly reduces the conductivity of the resulting heterostructure as reduced graphene oxide has carrier mobilities and conductivities 2–3 orders of magnitude lower than pristine graphene [22]. These methods also rely on harsh oxidizers, raising significant environmental concerns, and are incompatible with the large crystal size, high-quality graphene that has been produced through both sublimation of silicon carbide [23] and CVD deposition on copper [24]. To create the final solid heterostructure precipitate, these methods also require a long high-temperature step (~12 h, >500 °C) [16], which makes them impractical for large-scale synthesis. For these reasons, the production of large-scale MnO_x-graphene heterostructures and an analysis of its effects have not been seen in the literature.

In this work, a green, rapid (reaction times of ~1s) deposition of well-structured δ-MnO_2 on quasi-freestanding epitaxial graphene (QEG) silicon carbide (SiC) using a simple three-step electrodeposition process is demonstrated. The gas sensing suitability is validated, revealing an intercalation-based response to redox-active gasses. The synthesis of Mn_2O_3 and Mn_3O_4 from δ-MnO_2/QEG heterostructures is then demonstrated via thermal anneals in air and argon (Ar), respectively. The formation of these films is confirmed by Raman spectroscopy and X-ray photoelectron spectroscopy (XPS). The underlying graphene substrate was verified to be undamaged by the electrodeposition and thermal annealing processes. The formation of δ-MnO_2, Mn_2O_3, and Mn_3O_4 on QEG using a non-destructive novel, rapid, scalable, green synthesis method is presented.

2. Experimental

2.1. Material synthesis

Monolayer epitaxial graphene (EG) substrates were synthesized by sublimation of Si from the Si-face of semi-insulating 6H–SiC at 1580 °C in 75 Torr of Ar. During the temperature ramp to 1570 °C prior to growth, the SiC was etched in 5 slm of high purity H_2 at 150 Torr. The reactor is then cooled to 1050 °C in Ar. The synthesized monolayer EG was then hydrogen intercalated under an 80 slm H_2 flow in a 675 Torr H_2 environment for 60 min at 1050 °C, passivating the Si dangling bonds on the Si-face of SiC, promoting the buffer layer to an additional graphene layer, and reducing the electron-phonon coupling between the two materials to form a quasi-freestanding bilayer EG/6H–SiC heterostructures, as previously described [23].

δ-MnO_2 on QEG was then fabricated by electrodeposition using a three-electrode electrochemical cell with a QEG working electrode, a Pt mesh counter electrode, and a silver/silver chloride (Ag/AgCl) reference electrode. Manganese acetate (MnAC, Sigma Aldrich, 98 % purity) solutions, with concentrations from 100 mM to 2.5 mM, were used as the electrodeposition electrolyte. The MnAC solution was mixed immediately before the reaction to avoid oxidation, as indicated by the precipitation of brown MnO_2 particles in the solution. δ-MnO_2 was then deposited using a three-step reaction controlled by a potentiostat (Gamry 3000) at the redox potentials. Redox potentials are determined by cyclic voltammetry (CV), where potentials are cycled for five cycles with a −2.5 V–2.5 V potential window and a scan rate of 10 mV/s. According to CV, the oxidation potential was found to be 2.1 V, which was then lowered to 1.858 V for reaction to reduce the risk of graphene oxidation. The reduction potential of MnAC on QEG was determined to be −0.4 V. The potential for each step was 1.858 V, −0.4 V, and 1.858 V vs. Ag/AgCl with growth times from 920s to 0.5s.

After electrodeposition of δ-MnO_2, the sample was rinsed in 99 % isopropyl alcohol, deionized water, and dried in ambient conditions. The films were then annealed at temperatures from 50 to 500 °C in air and 500 °C in Ar for 2 h to produce Mn_2O_3 and Mn_3O_4, respectively. To determine the effect of high-temperature anneals on the crystal structure of δ-MnO_2, anneals in air and Ar ambient was conducted. Anneals in air were carried out on a commercial hot plate (ThermoFischer Scientific Cimarec). Anneals in Ar were conducted in a hot-walled furnace under 500 sccm Ar at 760 torr.

2.2. Material characterization

X-ray photoelectron spectroscopy (XPS), angle-resolved XPS, and Raman spectroscopy were used to analyze the structure and chemical composition of the as-grown and annealed thin films. The XPS measurements were collected in a Kratos Axis 165 X-ray photoelectron spectrometer operating in hybrid mode using monochromatized Al K α radiation ($\hbar\omega = 1486.7$ eV) at an anode power of 280 W. The survey spectra and high-resolution spectra were collected at pass energies of 160 eV and 40 eV, respectively, under a base pressure of 5×10^{-8} Torr. The angle-resolved XPS measurements were taken at angles of 0°, 45°, and 70° with respect to normal incidence. The effect of surface charging on the resulting binding energies was eliminated by shifting the advantageous carbon peak in the C1s to 284.8 eV. The high-resolution spectra were then deconvoluted using 30% Lorentzian Gaussian-Lorentzian line shapes and a Shirley background in the data analysis. The Raman spectra were collected with a Horiba LABRAM ARAMIS system using a 532 nm excitation source with a spot power of 14.7 μW. After the spectra were captured, they were then processed by subtracting a known QEG background and fitted using pure Lorentzian line shapes. The surface morphology was examined by a combination of scanning electron microscopy (SEM, Raith e_LiNE), tapping mode, and kelvin probe atomic force microscopy (AFM, Cypher ES Environmental). Kelvin probe force microscopy (KPFM) was conducted at a 50 nm pass offset and using a grounded sample and charged tip.

2.3. Gas sensing Measurments

Gas sensing tests were conducted in atmosphere with a constant flow of 500 sccm N_2 with variable humidity (RH) controlled via bubbling the N_2 through DI water (Owlstone Humidity Generator). The RH was calculated from the dewpoint using Magnus's form equations, where D_p is the dew point temperature measured at the outlet, and T is the ambient temperature (equ 1.) [25].

$$RH = 100 \times \left[\frac{e^{\frac{17.625 D_p}{243.04 + D_p}}}{e^{\frac{17.625 T}{243.04 + T}}} \right] \tag{1}$$

The redox active gas (NH_3 or NO_2) was added at a concentration of 10 ppm in N_2 and flow of 500 sccm for 30 min, before being turned off for 30 min to allow the sensor to recover. These measurements were taken in triplicate with the sample at 0 % and 100 % RH N_2 along with a bare QEG sample for comparison. The resistance measurement was taken by applying a 2 μA constant current to MnO_2 devices and monitoring the change in voltage. Measurements taken on bare QEG were taken at 20 μA to account for its significantly lower resistance.

For lower concentration NH_3 and NO_2 tests, a constant flow of 1000 sccm N_2 with a 100 % RH humidity was added to the cell, and then a variable flow of 10 ppm redox active gas (7.5 sccm, 30 sccm, 100 sccm, 300 sccm) was added to the environment for 30 min, before being turned off for 20 min to allow the sensor to recover.

3. Results and discussion

3.1. Growth of δ-MnO_2 compounds on QEG

Previous work has demonstrated that EG can be electrochemically functionalized with O^- groups. The functionalization of O^- was shown to be independent of defects on the EG surface, unlike H^+ functionalization [26]. With seeding the QEG surface with O^- possible, a three-step electrodeposition process was used to deposit δ-MnO_2 on QEG, first starting at the oxidation potential. Seeding the surface with O^- groups enables nucleation sites for the formation of MnO_2. The second step occurs at the reduction potential to deposit Mn $^+$ ions onto the O^- groups before the final step deposits additional oxygen to form δ-MnO_2. Using cyclic voltammetry, as discussed in our previous work [8], the oxidation potential was found at 1.858 V and the reduction potential at –0.4 V. Following electrodeposition, a semi-transparent brown film formed on the QEG surface with large grain sizes (>100 μm) and distances between grains, from grain boundary to grain boundary (~1 μm) penetrating to and revealing the underlying QEG substrate. To observe how varying growth conditions affect the quality and thickness of the deposited δ-MnO_2, the first pulse duration, third pulse duration, solution molarity, and total growth duration were varied to determine optimal growth conditions, which are detailed in Table 1.

3.2. Characterization of the as-grown δ-MnO_2 thin films

To confirm the formation of δ-MnO_2 on the QEG substrate, the materials were characterized by a combination of Raman spectroscopy, XPS, AFM, and SEM. These techniques allow us to probe both the material quality and the surface characteristics of the resulting films, which allows us to determine the optimal growth conditions to produce high-quality δ-MnO_2.

Raman spectroscopy allowed us to confirm the formation of δ-MnO_2 as it has a distinct Raman spectrum from other materials and MnO2 polymorphs [27]. Group theory calculations predict nine active Raman bands in δ-MnO2 (3 Ag+6 Bg). The most intense of these bands have been reported at 500-510 cm^{-1}, 575-585 cm^{-1}, and 620-650 cm^{-1} [27–29]. These modes have generally been assigned to the Mn–*O*–Mn deformation mode, the Mn–*O*–Mn stretching mode in the basal plane, and the Mn–*O*–Mn stretching mode of the characteristic octahedra, respectively [6]. Additional low-intensity peaks at 710-730 cm^{-1}, 610-630 cm^{-1}, and 390-410 cm^{-1} have been reported in the literature but have no physical assignment at this point [27–30]. α-MnO_2 or 2x2 tunnel phase has a similar Raman spectrum, but clear differences appear in the low IR region where α-MnO_2 has a strong band at 180 cm^{-1}, of similar intensity to its Mn–*O*–Mn peak at 500 cm^{-1}, related to its tunnel structure [27,31–39]. By contrast, δ-MnO_2 has a low-intensity band at 120-130 cm^{-1} related to the vibration of interlayer H_2O molecules, and does not contain a strong band below 200 cm^{-1} [27,30,32,40–44]. In the observed Raman spectra (Fig. 1), three characteristic Raman peaks at 501 cm^{-1}, 576 cm^{-1}, and 652 cm^{-1}, as well as a weak band at 120 cm^{-1}, were observed. This indicates that δ-MnO_2 on QEG was formed. Also visible in the Raman [32]spectra was a weak peak at 617 cm^{-1}, attributed to defect phases in the MnO_x structure [28], which was utilized to track material quality with changing growth conditions. The Raman spectra also indicated that the epitaxial graphene was undamaged as there was no formation of a visible D peak, and the 2D peak FWHM remained at 66 cm^{-1}, indicating the maintenance of the bilayer character of the epitaxial graphene film [23].

To further verify the formation and quality of the as-grown δ-MnO_2, XPS was used due to its high sensitivity to elemental composition, as a simple linear relationship has been found between the 3s peak splitting and the formal oxidation state of manganese [46]. In the survey scan of our as-grown δ-MnO_2, the only significant elements found were Mn, O, Si, and C, consistent with water-stabilized birnessite, as opposed to K or Na type birnessite (Fig. 2a). Additionally, our observed Mn 3s spectra exhibited a peak splitting of 5 eV, indicating a formal oxidation state of +3.33 (Fig. 2b). Using this in combination with the collected Raman spectra, the optimal growth conditions for high-quality thin films were determined.

To characterize the surface morphology of the resulting thin films, a combination of SEM and AFM was used to obtain surface morphology, roughness, and approximate thickness of the deposited thin films. SEM analysis of the film revealed that the film is made of rectangular microplatelets with sizes of approximately 50 μm × 30 μm (Fig. 3a). The long axis of these rectangular microplatelets was generally perpendicular to the SiC step edges (Fig. 3b). This indicates that the formation of these platelets was related to a lattice strain between the δ-MnO_2 and SiC. This is consistent with the known lattice mismatch between 6H–SiC and δ-MnO_2, which share a hexagonal crystal structure with lattice constants $a = 3.08$ Å [6] and $a = 2.84$ Å [47], respectively. This is further corroborated by the fact that these cracks do not form immediately but form during the drying procedure. Higher magnification SEM images indicated that the surface of these microplatelets is made up of randomly oriented nanofibers, with widths of approximately 10 nm. As active surface area is a key predictor of transition metal oxide performance, this nanofibrous surface is highly desirable in the formation of MnO_2- QEG heterostructures (Fig. 3c). AFM imaging of the heterostructures confirmed that they were formed into microplatelets made up of nanofibrous nanoparticles. In addition, AFM height profiles indicated that these films were approximately 50 nm thick, or ~26 layers of δ-MnO_2 manganese dioxide (Fig. S1), and had a surface roughness of 2.5 nm in the optimal growth condition (Fig. 3d).

3.3. Determination of the optimal growth conditions

Electrochemical synthesis of materials is very sensitive to relatively minor changes in growth conditions, which allows us to control and tune the deposited heterostructure by varying these conditions. Using this method, the aim was to find the optimal growth procedure to produce high-quality thin films, which are considered to be the thinnest, lowest roughness film possible with a relatively high defect density [43]. The high defect density is desirable as it improves the reactivity of the resulting films, and the low thickness improves charge transfer to the underlying graphene sheet. To achieve this, we varied the pulse durations, and the solution molarity, in several series, which are described below in Table 1.

To observe the change in material quality with varying growth

Table 1
Growth variables for the electrochemical synthesis of MnO_2 on QEG.

Variable Swept	First Pulse Duration (s)	Second Pulse Duration (s)	Third Pulse Duration (s)	Total Duration (s)	Solution Molarity (mM)
Third Pulse Duration	600	20	300 to 20	920 to 620	100
First Pulse Duration	600 to 20	20	0	620 to 40	100
Solution Molarity	20	20	0	40	100 to 5
Total Duration (Ratios Constant)	15 to 0.5	15 to 0.5	7.5 to 0.25	37.5 to 0.5	20
Solution Molarity	0.5	0.5	0.25	1.25	20 to 2.5

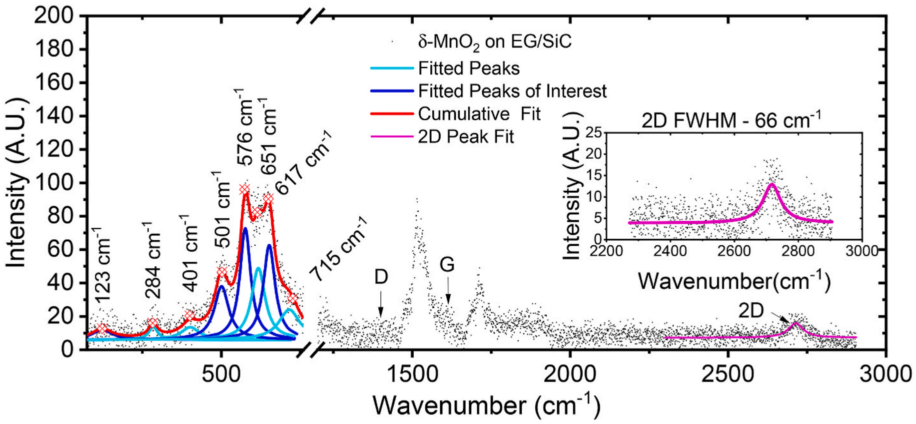

Fig. 1. Raman spectra of δ-MnO_2 on QEG substrates. Visible in the spectrum are the characteristic peaks at 651 cm^{-1}, 576 cm^{-1}, 501 cm^{-1}, and 123 cm^{-1}, which indicate the formation of δ-MnO_2. A weak peak is also observed a 617 cm^{-1} which is associated with defected MnO_x materials, which we tracked to determine the material quality of the resulting films. The mixed peaks observed at 1520 cm^{-1} and 1713 cm^{-1} are related to the 6H–SiC substrate, on which the epitaxial graphene was grown [45].

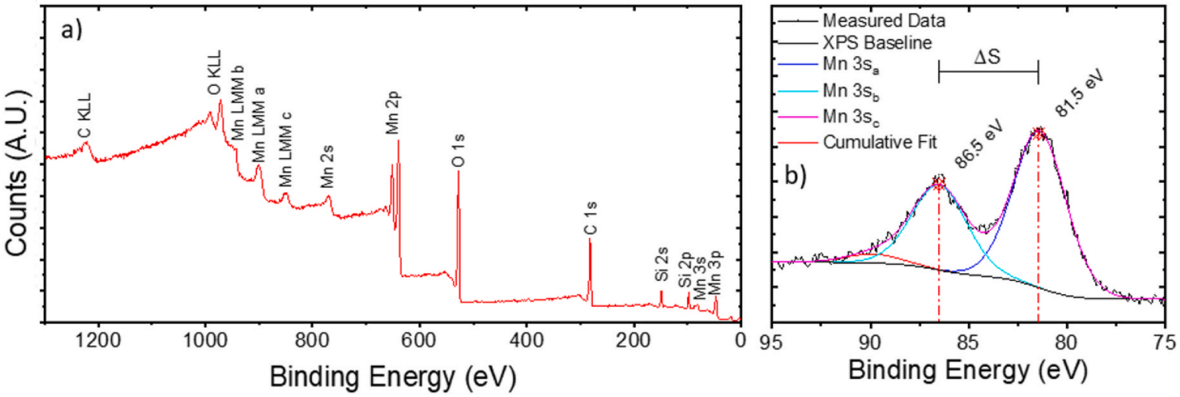

Fig. 2. XPS (a) survey spectra, (b) 3s region spectra of δ-MnO_2 on QEG substrates. Observed here is a 5 eV separation between the Mn 3s peaks, which using the linear relation between splitting and formal oxidation state (8.965-1.126ΔS) indicates a formal oxidation state of +3.33. A lack of alkali metal ions indicates the absence of a high defect density water-stabilized birnessite phase.

conditions, the change in the ratio between the 575-585 cm^{-1} peak, which is related to basal plane phonon modes in the layers (V_1), and the peak at 610-620 cm^{-1}, related to MnO_x defects in the structure (V_b) was tracked in the Raman spectra. This gives insights into the structural order in relation to the defect quantity in the material. The variation of Mn formal valence confirms these observations, which were well-correlated to the change in V_1/V_b ratio, indicating the veracity of this method. was also followed. The surface thickness and roughness were also monitored to improve material quality.

First, the third pulse duration was varied, with decreasing third pulse duration resulting in increases in the V_1/V_b ratio as well as increases in the formal valence. This indicates that shorter third pulses improve material quality. However, upon removing the third pulse entirety, both metrics decrease (figure S2a), indicating that a short, nonzero third pulse is desirable for good growth. It was also found that for third pulse durations longer than 60 s, a thick black "crust" layer formed on the surface. Upon reducing the third pulse time to 60 s, the entire film delaminated during the growth (figure S2b), implying that the crust layer may have been formed by the delaminated film adhering to new growth on the surface. We also observed that these films had a thickness greater than 10 μm, which we found to be undesirable.

No strong correlation between the first pulse duration and film quality was observed when a third pulse was omitted. The variation of Raman ratios and formal valence indicated that its effect on material quality was inconsistent (figure S3a). However, reduced first pulse duration was very well correlated ($R^2 = 0.92$) with film thickness and film roughness, with a decrease in thickness from 1200 nm to 100 nm at the lowest duration (figure S3b). As a result, a first pulse duration of 20 s was selected for growth optimization.

To reduce the film thickness further the solution molarity was decreased. Reducing the solution molarity decreased the Raman ratio and formal valence until the film began to break up into islands at concentrations below 20 mM, which led us to select 20 mM as the optimal solution molarity for high-quality films (figure S4a). Similar to the first pulse duration, the film thickness is highly correlated ($R^2 = 0.96$) with solution molarity, reducing from 100 nm to 50 nm with a reduction from 100 mM to 20 mM (figure S4b). In addition, as can be seen, by the surface roughness, the films degrade significantly at concentrations below 20 mM.

After these optimizations, the third pulse was reintroduced to improve film quality and then the total duration of growth was varied, maintaining a pulse duration ratio of 1:1:0.5 in an attempt to further reduce film thickness. The addition of the third pulse increased film thickness and manganese formal valence. Upon reducing the total duration, the V_1/V_b ratio and formal valence increased, indicating improved material quality until 1.25 s growth, after which the increases began to saturate (figure S5a). The thickness and surface roughness followed a similar trend to the solution molarity, with the reduced duration being highly correlated with thickness and roughness reduction, with the final film saturating at a thickness of 50 nm,

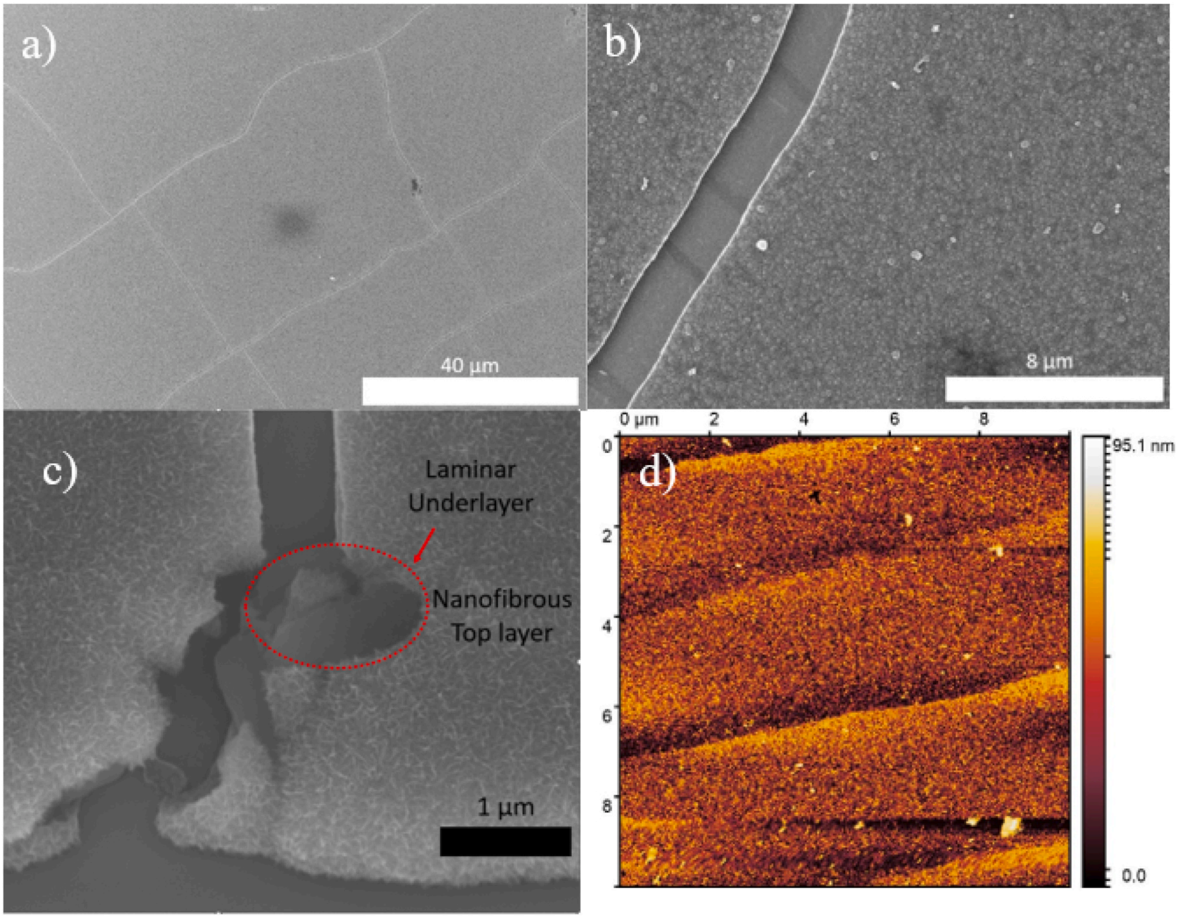

Fig. 3. SEM (a–c) and AFM (d) images of δ-MnO_2 on QEG. The SEM images were taken at (a) 1 kx and (b) 5 kx (c) 20 kx. They indicate the surface is made up of rectangular microplatelets greater than 40 μm by 40 μm. The higher magnification image reveals that these cracks are perpendicular to the graphene step edges, and the surface is made up of nanofibrous particles, but underneath is a laminar δ-MnO_2 structure. AFM imaging (10 μm by 10 μm) indicated the surface was quite smooth, with a surface roughness (Ra) of ~2.5 nm.

approximately 26 layers of δ-MnO_2, and roughness of ~2.5 nm.

Based on these results, growth with pulse durations of 500 ms, 500 ms, and 250 ms and solution molarity of 20 mM resulted in the highest quality films, with δ-MnO_2 films ~55 nm thick and 3.33 formal valence, indicating the formation of a very thin film of δ-MnO_2 with high defect density and no stabilizing cations, which to our knowledge has not been reported thus far.

4. Exploration of the growth mechanism of δ-MnO_2 on QEG

As previously noted, the thickness of the grown films was limited to 50 nm or above, and attempts to reduce this via reducing the deposition duration or solution molarity led to film degradation. This, while limiting the growth, allowed us to observe parts of the growth mechanism by reducing the solution's molarity. As a result, with our optimal growth process, we reduced solution molarity and observed the surface via AFM and SEM. As the solution molarity was reduced to 5 mM, significant pinhole defects formed in the film, most dense on the SiC terraces and least dense on the step edges of the material (Fig. 4a). As the molarity was reduced further to 2.5 mM, a film was no longer formed, but a large number of 50 nm islands, which were densest on the SiC step edges, of MnO_2 were deposited on the surface. This indicated that the primary growth mode of the film was the deposition of 50 nm islands that then grow outwards and merge to form the film (Fig. 4b). This is consistent with the previous SEM images showing clear nanoparticles on the surface of the film. SEM images confirmed this growth mechanism and corroborated that island nucleation was favored along the step edges., with the growth being nearly a contiguous film on the step edges and growing into the terraces (Fig. 4c). This indicated to us that the electrochemical deposition is enhanced by the presence of dangling bonds, as the favorable nucleation sites are the step edges, which have a higher incidence of dangling bonds than the terraces [12]. Additionally, we fabricated patterened QEG ribbons via CF_4 etching to test the importance of QEG on the electrodeposition process. SEM images of this growth illustrate a strong conformality of the δ-MnO_2 to the patterned QEG surface, confirming we are using an electrodeposition method as opposed to ionic precipitation (Fig. S6).

4.1. *Verification of the epitaxial growth of δ-MnO_2 on QEG*

The nanofibrous character of the δ-MnO_2 surface, as was observed in the SEM, raises questions about whether the formed material is layered as expected or similar to other nanoflowers and nanourchin structures reported in the literature in other materials. XPS can be used to probe this question as it is surface sensitive and can determine the manganese formal valence via the Mn 3s, as well as provide insight into oxygen bond terminations and defects via the O1s region of the spectra. This can then be combined with angle-resolved methods to observe variations in defects between the bulk and the surface by observing the variation in Mn 3s and O1s spectra at glancing and normal incidence to the surface. To examine this, we used an unoptimized thin film, but the similarity in morphology indicates the result should be similar to the optimized growth. At normal incidence, the Mn 3s peak splitting was found to be 5.15 eV (Fig. 5a), yielding an Mn formal valence of 3.16 in bulk. When

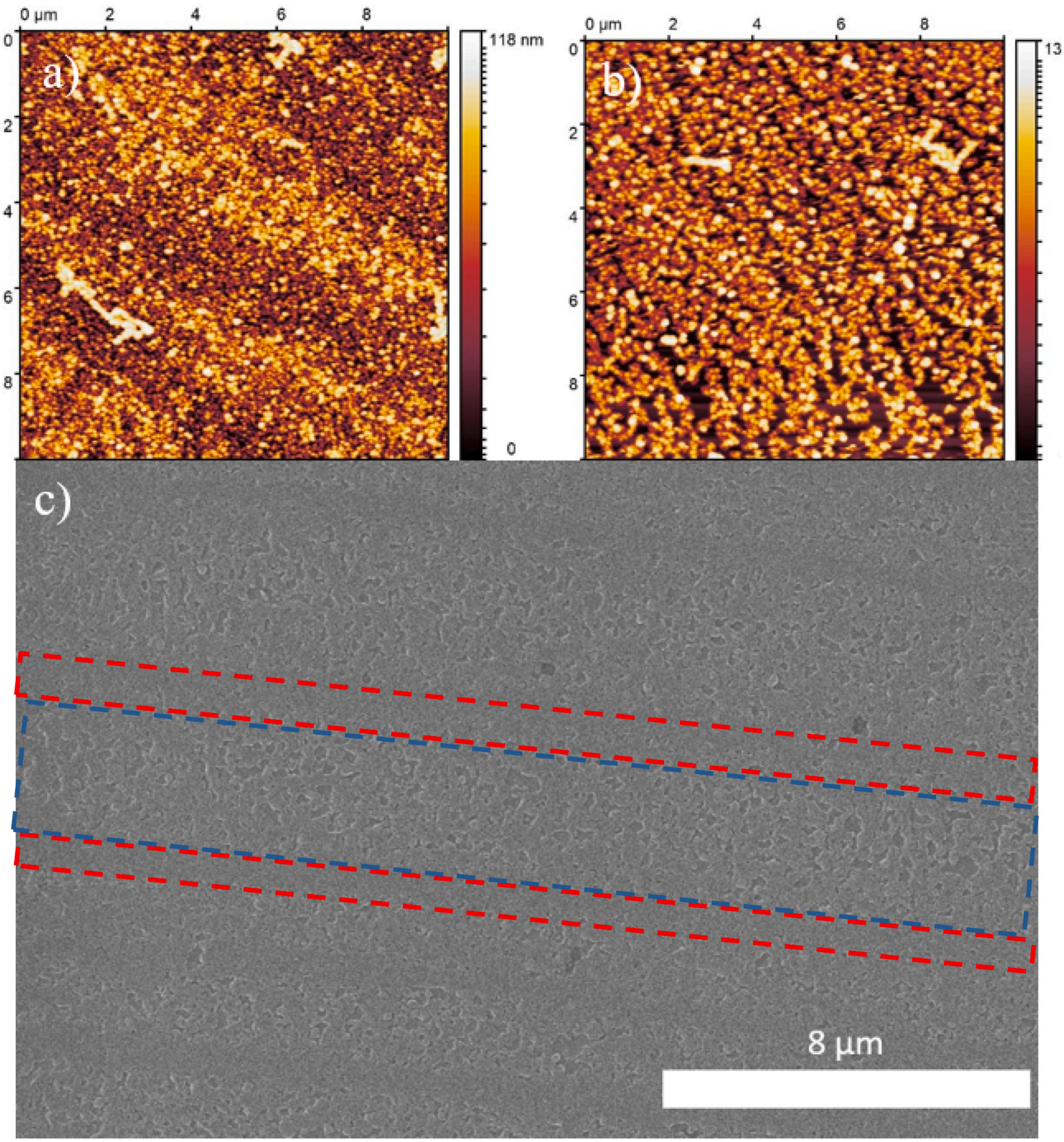

Fig. 4. AFM Height images of deposition with (a) 5 mM (c) 2.5 mM MnAc and (c) SEM image of deposition with 5 mM MnAc. It can be seen that as the solution molarity is reduced to 2.5 mM, the film becomes individual islands with a thickness of ~50 nm. At 5 mM, a film can still be seen, but it is dominated by pinhole defects. This is confirmed in the SEM, as is the favored nucleation site of the graphene step edges. The red outlined regions are step edges, while the blue outlined region is the terrace between these regions.

taken at glancing incidence, the Mn 3s peak splitting was found to be 5.26 eV (Fig. 5c), yielding an Mn formal valence of 3.04 in the surface, indicating that the surface contains a significantly higher $Mn^{+2/+3}$ defect density than the bulk of the film. An analysis of the O1s spectra corroborates this. At both normal and glancing incidence, the O1s spectra contain three components, the Mn–*O*–Mn bond at 529.9 eV, the Mn–*O*–H bond at 531.4 eV, and the H–*O*–H bond at 532.8 eV, which is consistent with water stabilized δ-MnO_2 [48]. However, the contribution of the three components varies significantly between glancing and normal incidence. At normal incidence, the Mn–*O*–H contributes 37.8 % of the total O1s spectral area, while at glancing incidence, it contributes 46.1 % of the O1s spectral area. This indicates that the surface contains a significantly higher number of $Mn^{+2/+3}$ defects, consistent with the Mn 3s analysis, and that many of these defects are terminated in hydroxyl groups (Fig. 5 b,d). Due to the material surface's highly defected and hydroxylated nature, we would expect the surface reactivity to be enhanced, which is desirable for most manganese applications.

The nanofibrous character of the surface brings into question whether the growth was epitaxially planar, as we had anticipated, or a less ordered deposition had occurred. To explore this possibility we conducted SEM to observe defects on the as-deposited surface. This revealed plate-like features underneath the nanofibrous surface (Fig. S6), indicating the growth was epitaxial. From this, we concluded the nanofiberous surface was due to the formation of MnOOH during deposition, on top of the laminar δ-MnO_2. We then confirmed this by conducting mechanical exfoliation of the planar film, as epitaxial layered materials can be readily thinned by transfer with a simple adhesive (i.e. scotch tape) [49]. Transfer of optimized films led to a mixture of blue-white flakes, and blue transparent flakes. AFM analysis of these exfoliated films revealed that the transparent exfoliated flakes

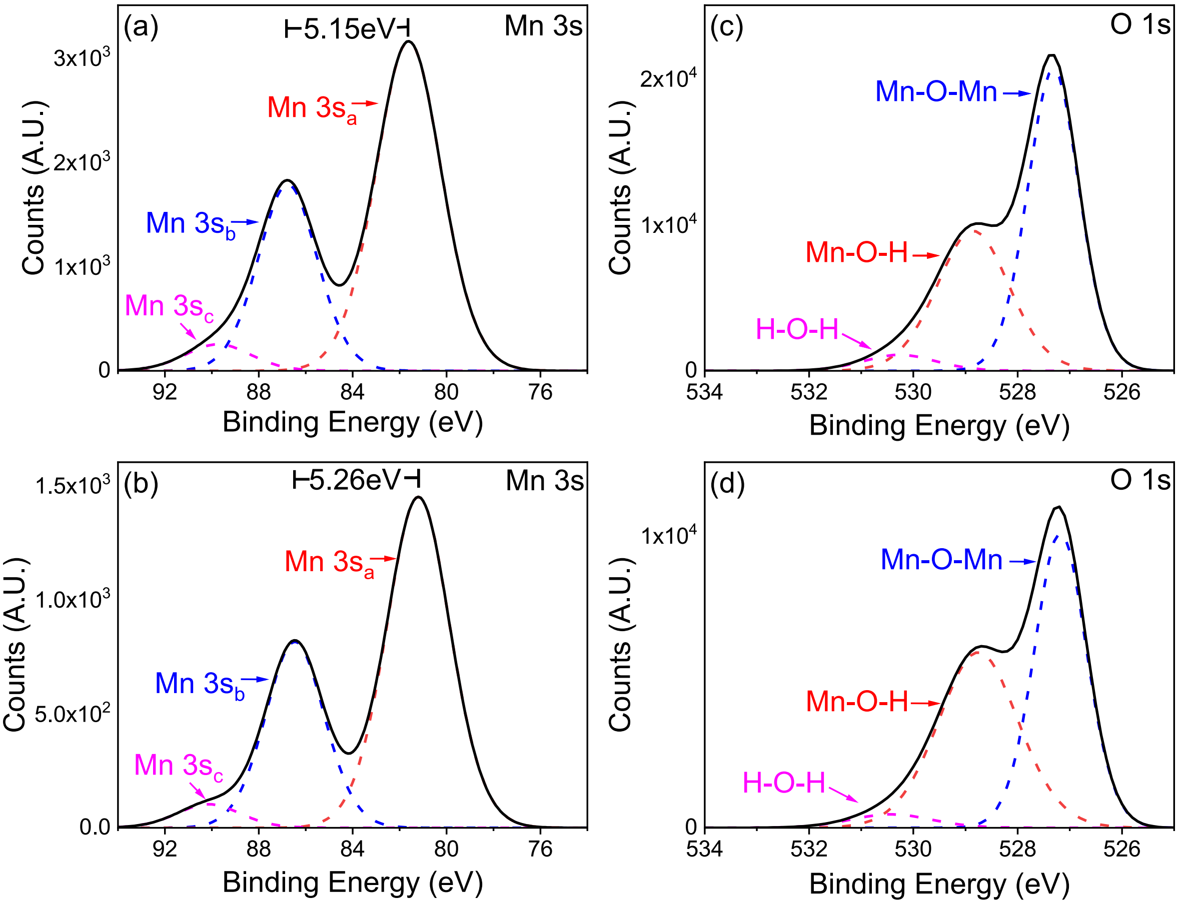

Fig. 5. Angle-Resolved XPS of δ-MnO_2 of the (a,b) Mn 3s and (c,d) O1s at (a,c) 0° and (b,d) 70° from normal incidence. The increase in Mn 3s peak splitting and Mn–*O*–H contribution to the O1s spectra at higher angles indicates that the surface has a higher defect density and a larger number of hydroxylated Mn^{+3} sites.

had surface roughness less than 1 nm (Fig. 6a), and the thinnest observed flake was ~5 nm (Fig. 6b), while the phase image indicated that these flakes were generally uniform (Fig. 6c). This indicates that the δ-MnO_2 growth was epitaxial and planar, as this exfoliation behavior is similar to other epitaxial layered materials such as transition metal dichalcogenides [49]. This is in good agreement with the XPS data that indicates despite the nanofibrous surface, the growth is generally planar and epitaxial in nature.

4.2. *Determination of the potential barrier between δ-MnO_2 and QEG*

As stated previously, a key advantage of the δ-MnO_2 QEG heterostructure is the conductivity enhancement of the δ-MnO_2 by the QEG. The scale of this is, in part, determined by the potential barrier formed between the materials, which limits carrier flow. This potential barrier also has implications for the properties of devices formed with this structure and is therefore important to determine. To do this, Kelvin force probe microscopy (KPFM) was conducted on the heterostructure, which determines the work function of the materials via a capacitive effect [50]. The KPFM indicated that the manganese dioxide exhibited a p-type doping effect on the QEG, driving its work function from 4.8 eV [51] to 4.95 eV (Fig. 7 a-b). It also indicated that a 300 meV potential barrier was formed between the MnO_2 and the QEG, with the MnO_2 work function being 5.25 eV. The small size of this potential barrier allows for high-speed charge transfer between the graphene and the MnO_2 and therefore improves reaction kinetics in the resulting heterostructure [8]. As charge transfer drives a majority of MnO_x applications, we believe this is desirable for future device applications.

4.3. *Gas sensing results of δ-MnO_2-QEG heterostructures*

Following the determination of the potential barrier between QEG and δ-MnO_2 we evaluated its impact on the gas sensing results of the material. Previously, we have reported on the detection of redox-active gasses by δ-MnO_2 on non-intercalated epitaxial graphene using unoptimized films [8], however, the effects of the optimization of the material growth, and the H_2 intercalated substrate were unexplored. To examine the effects of these changes we first grew the optimized film on patterned 100 μm × 8 mm QEG ribbons, taking advantage of the fact that δ-MnO_2 does not grow on the semi-insulating SiC substrate to produce separate devices. The purpose of utilizing ribbons was to allow for the intercalation of gas molecules into the interlayer of the epitaxial film and improve active surface area [29]. These devices were then exposed to 5 ppm NH_3 and NO_2 with a variable humidity N_2 background to observe the effect of water on the sensor performance.

The response of these sensors (Fig. 8) shows a similar enhancement in response/recovery (τ_{res}/τ_{rec}) as other TMO-graphene heterostructures at room temperature, with a reduction of τ_{res}/τ_{rec} to the order of 1000–2000 s, 1498.7 ± 49.4 s/1485 ± 43 s for 5 ppm NO_2 (Fig. 8a), and 867.3 ± 161.1 s/945.5 ± 110.5 s for 5 ppm NH_3 (Fig. 8b) in dry N_2 [52]. In addition, it also shows exceptional SNR, with a 40.7 ± 2.1 dB response to NO_2, and a 46.8 ± 0.9 dB response to NH_3, as noise is a significant limiting factor on LOD and the ability of response to be amplified indicating that despite the relatively low responsivity of the sensors (1.94 ± 0.23 % to NH_3 and -0.97 ± 0.20 % to NO_2) they can be amplified to generate a much higher signal using relatively simple circuity [53].

The effect of humidity on the system, however, was not similar to

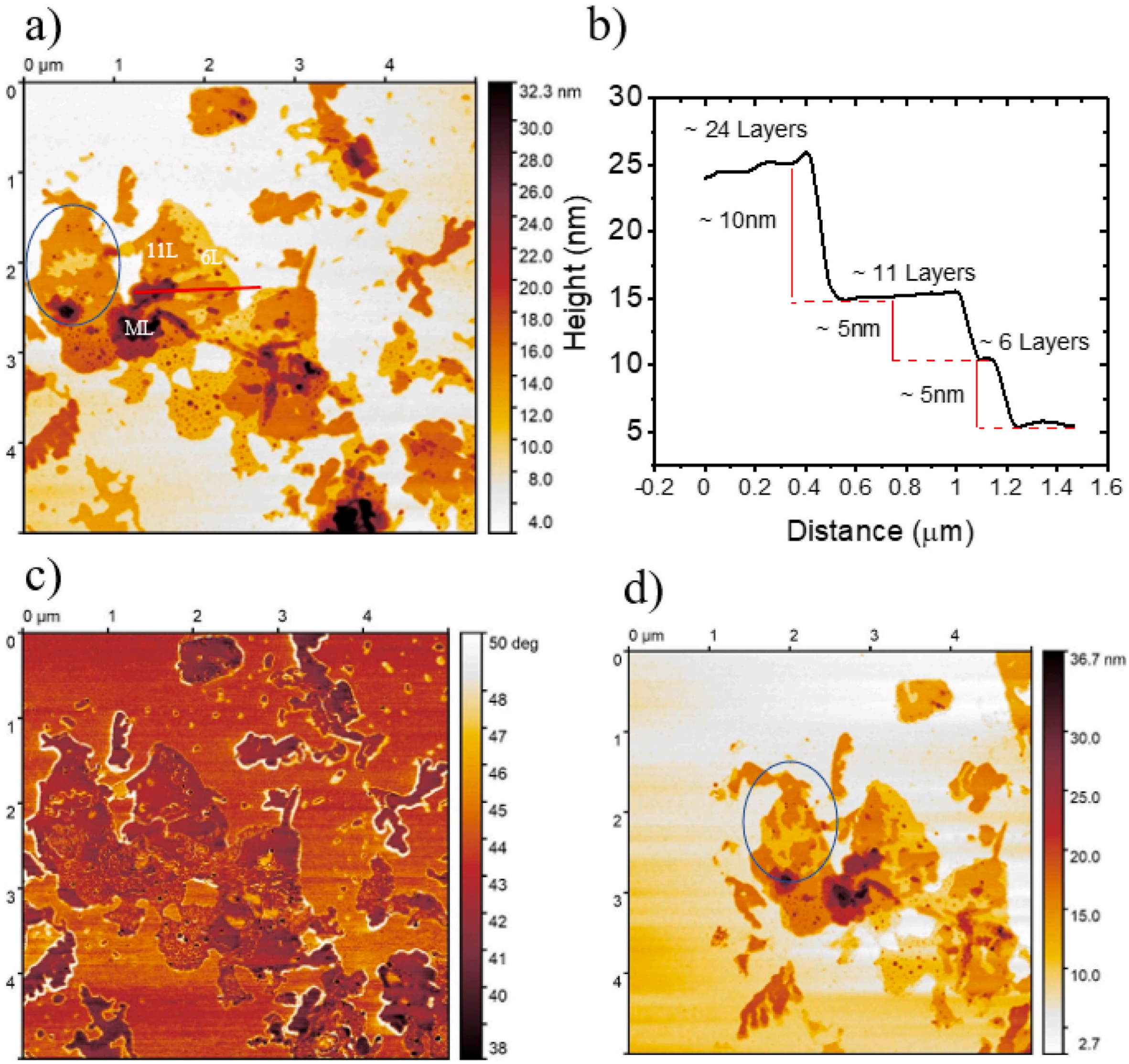

Fig. 6. AFM (a,d) height and (c) phase images of mechanically exfoliated δ-MnO_2 on SiO_2. The height images indicate that a large number of unordered flakes were transferred from the EG/SiC substrate. These flakes are shown to have layer thicknesses spanning from approximately 6 layers to over 30 layers at the thickest point, which can be seen from the extracted profile (b). The general flatness of these flakes confirms their epitaxially layered nature. The phase image shows three distinct phases. A high phase is associated with adhesive residue from the transfer, the substrate phase, and the phase of the transferred material. That the transferred material has a distinct and consistent phase from the adhesive indicates we are seeing transferred δ-MnO_2. The presence of particulates on the surface of the flakes does raise concerns, however, continued scans of the same region indicate that the flake layers are very fragile and damaged by the AFM process, as demonstrated by the reduction in the size of the 11-layer region between (a) and (d). This indicates that these particles are caused by the destruction of the top layers by interaction with the environment.

what would be expected in transition metal oxide sensors [52,54,55]. Traditionally, water acts as a competitor for the active sites on TMO gas sensors, which reduces the responsivity and limits the other sensing characteristics of TMO and TMO heterostructure sensors. But in our devices the presence of water improved responsivity and τ_{res}/τ_{rec} time for NO_2 to -3.76 ± 0.33 % and 1368.7 ± 66.7 s/418.3 ± 300.7 s respectively, as well as making the response far more stable. In addition, on the NH_3 response, a secondary response of the opposite sign was observed in the presence of water, with a τ_{res}/τ_{rec} of 66.4 ± 41.7 s/7.5 ± 0.03 s, and a responsivity of -0.26 ± 0.03 %, which we have not seen described in the literature.

An explanation for this response can be found in the structure of water-stabilized birnessite. In this material, two layers of defected and negatively charged MnO_{2-x} are compensated for and kept stable by polar H_2O and Mn^{+2} ions in the interlayer [41]. In this structure, NO_2, which will be reduced to NO_2^- cannot enter the interlayer, as it would destabilize the structure and can only react with the surface. This causes our traditional P-type redox gas sensing response. However, in the presence of high atmospheric water content, the ability of H_2O to screen ionic molecules allows for it to enter the interlayer region, significantly enhancing the response [56]. This also provides an explanation for why the τ_{rec} reduces to $\frac{1}{3}$ that of a dry environment, as the unstable NO_2^- in the interlayer is removed significantly faster than traditional redox recovery. The ability of water to facilitate interlayer intercalation is also implicated in the secondary response in NH_3. In both 0 % and 100 % RH tests, the NH_3 τ_{res}/τ_{rec} and responsivity are similar, changing to 585.8 ± 213s/1088.9 ± 89.4s and 1.45 ± 0.2 %. However, in the presence of high atmospheric water, there is a secondary response of opposite polarity (R_1). This is explained by the fact that NH_3, which oxidizes to NH_3^+ in the sensor, can readily intercalate into the negatively charged interlayer without the assistance of water. However, in an excess water environment, it can also force out excess water molecules, taking their

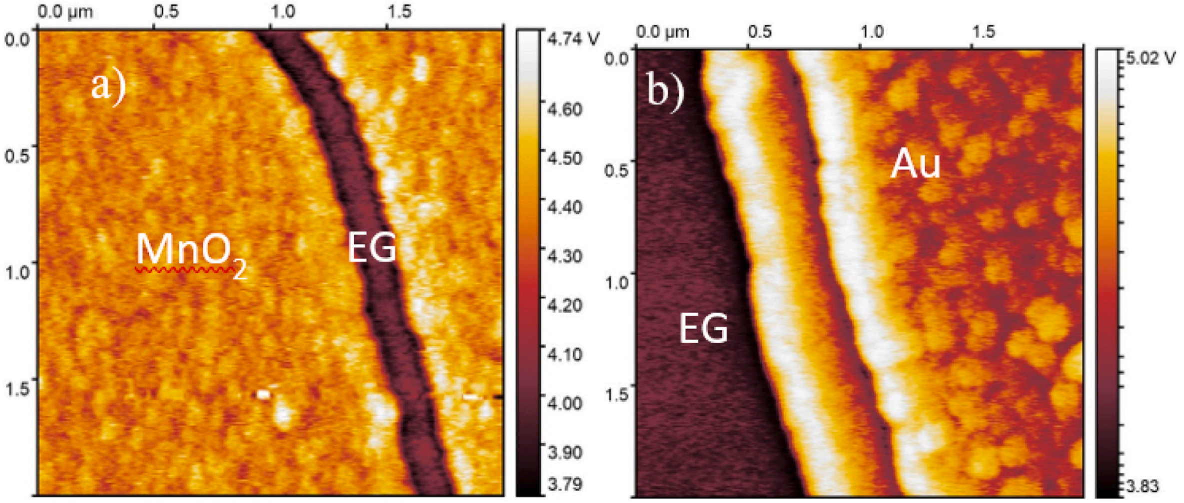

Fig. 7. Kelvin probe force microscopy images of the (a) MnO_2/EG junction and the (b) EG/Au junction. In (b) there is a visible 150 meV barrier between the EG and the Au ($\Phi = 5.1$ eV) and in (a) there is a 300 meV barrier between MnO_2 and EG. This indicates p-type doping from the MnO_2 as the EG has a modified work function of 4.95 eV and the MnO_2 has a work function of 5.25 eV.

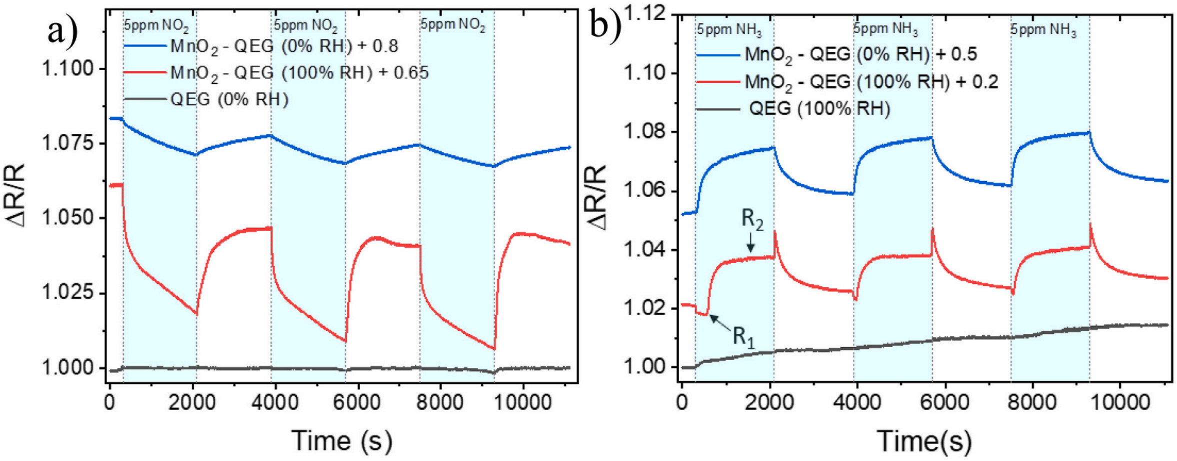

Fig. 8. Gas sensing response of 100 µm wide ribbons of δ-MnO_2-QEG and bare QEG to (a) NO_2 and (b) NH_3 at variable dilution humidities. In both responses, it can be seen that the MnO_2 offers significant enhancement over the bare graphene and that the presence of water significantly improves both the response/recovery times and responsivity of the δ-MnO_2 heterostructures. Additionally in the NH_3 test two distinct responses are observed in the presence of water (R_1 and R_2), indicating it allows for an intercalation effect in the sensor response.

place in stabilizing the structure, before the traditional redox activity takes over. This helps to provide evidence of intercalation response in the sensors, and a path forward on intercalation-based gas sensing on molecular size and charge.

By varying the concentration of the input gas, we were able to determine that the novel two-part NH_3 response was maintained even at very low concentrations (7.5 ppb), where it quenched the positive response entirely. NO_2 also showed a similar but reduced response, as expected, from the decrease in concentration (Fig. S9).

4.4. Transformation of δ-MnO_2 compounds on QEG to MnO_x compounds via heat treatment

The literature indicates that δ-MnO_2 will readily reduce to a lower oxidation state of manganese oxide under mild annealing conditions of approximately 500 °C [57]. This transformation is also tunable by varying the oxygen content of the annealing environment, with low oxygen content increasing the reducing effect of the annealing process [57]. As the oxygen intercalation temperature of QEG on SiC is ~600 °C in air [58], the transformation of as-deposited δ-MnO_2 to Mn_2O_3 and Mn_3O_4 can be achieved without significantly damaging the underlying epitaxial graphene surface or replacing hydrogen intercalations with oxygen. To confirm this transformation with our films, we annealed the as-deposited δ-MnO_2 in air for 2 h, under temperatures from 50 °C to 500 °C, to observe the transformation to Mn_2O_3. We then annealed as-deposited δ-MnO_2 in Ar for 2 h at 500 °C to observe the transformation of the film to Mn_3O_4. By this method, we were able to generate Mn_2O_3 and Mn_3O_4 on non-defected graphene, in this case, QEG, which to our knowledge, has not been previously reported.

4.5. Characterization of the annealed MnO_x thin films

The Raman spectra of MnO_x compounds are all quite distinct, which allows us to observe the transformation of the material from δ-MnO_2 to Mn_2O_3 and Mn_3O_4 easily via this method [6,50]. Raman also allows us to determine the integrity of the underlying QEG, as its Raman spectra are strongly related to its structural order and material quality [23]. This makes Raman a powerful tool for analyzing these annealing processes.

During the initial anneals in air, significant changes in the Raman spectra were observed. For annealing temperatures under 100 °C, the characteristic δ-MnO_2 was maintained with limited changes in the V_1/V_b ratio. However, as the temperature was increased beyond this to 200 °C, the Raman spectrum of the films degrades into a combination of various MnO_x compounds (figure S10a). This is seen by the enhancement of the peak at 611 cm^{-1} and its shift to 630 cm^{-1}, which is consistent with the formation of γ-Mn_2O_3, a heating-based decomposition product in the Raman spectrum [6]. As the temperature is further increased from 200 °C to 400 °C, the film changes significantly, with the Raman spectrum reforming sharp peaks, indicating the partial recrystallization of the film (figure S10b). After the annealing temperature is increased further to 500 °C, the film recrystallizes completely, containing only sharp peaks, indicating the formation of a lower oxidation state manganese product. In this Raman spectrum between 100 and 750 cm^{-1}, we observed 4 strong bands, located at 200 cm^{-1}, 319 cm^{-1}, 650 cm^{-1}, and 705 cm^{-1}. This is consistent with the formation of bixbyite or α-Mn_2O_3 in the film [59] (Fig. 9a). The lack of broad weak bands in these regions indicates that the amorphous MnO_x compounds have been fully transformed to α-Mn_2O_3 producing a high-quality film. At 500 °C, the region between 1200 and 3000 cm^{-1} was analyzed to determine if the transformation from MnO_2 to Mn_2O_3 had damaged the graphene. In this region, a slight D-peak was observed, indicating some damage was done to the underlying graphene, but the D/G ratio was 0.11 indicating the damage was minor (figure S11a). The 2D peak maintained a FWHM of ~67 cm^{-1}, indicating the bilayer character of the film and, therefore, its hydrogen intercalation quasi-freestanding nature maintained during the annealing process [23].

Following a 2-h anneal in Ar at 500 °C, significant changes in the Raman spectra were also observed, indicating a transformation of the δ-MnO_2 into Mn_3O_4. This was evidenced by the appearance of strong Raman bands at 660 cm^{-1}, 374 cm^{-1}, and 320 cm^{-1}, consistent with Mn_3O_4, and the removal of all other peaks from the spectra [6] (Fig. 9b) Additional analysis of the graphene, in the region from 1200 to 3000 cm^{-1}, indicated its quality was maintained as no D-peak was observed (figure S11b) and the FWHM of the 2D peak was 60 cm^{-1} [23]. This confirms that the process did not damage the underlying graphene substrate and demonstrates the growth of thin films of δ-MnO_2, α-Mn_2O_3, and Mn_3O_4 on EG/SiC without damaging the underlying graphene substrate.

The surface morphology of the film changed with annealing in air. As the surface was annealed at low temperature (50 °C–100 °C), nanoplates replaced the nanofibers originally observed on the surface, with a nearly perpendicular angle relative to the surface (figure S12a). We believe that these platelets are the result of the nanofibers merging as the surface is annealed. As the temperature increases beyond 100 °C, the nanoplatelets change with their size increasing and their angle relative to the surface becoming shallower (figure S12b). This trend continues with increasing temperature (figure S12c). When the temperature is increased to 500 °C, a significant change in the surface morphology was observed, which accompanies the crystallization to Mn_2O_3. At this temperature, the surface becomes nanoporous, with pores approximately 10 nm in diameter (Fig. 10a). We believe this is a continuation of the previous process, with the nanoplatelets merging together to form a porous film. A change was observed by SEM accompanying the transformation to Mn_3O_4. After the transformation, the surface became made up of nanocubes, connected by rough nanowalls, with cube sizes on the order of 100 nm (Fig. 10b). AFM imaging of the heterostructures was

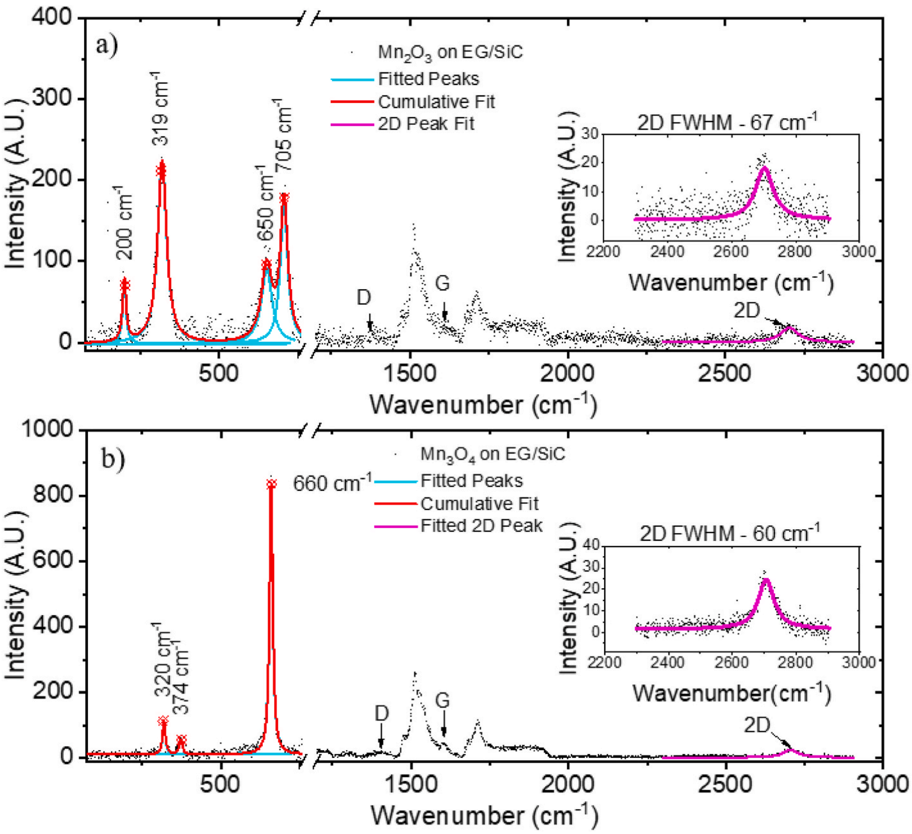

Fig. 9. Raman Spectra(a) Mn_2O_3, (b) Mn_3O_4 on QEG. After annealing, in air(b) the appearance of peaks at 200 cm^{-1}, 319 cm^{-1}, 650 cm^{-1}, and 705^{-1}cm indicates the formation of α-Mn_2O_3. After annealing in Ar (b) the appearance of peaks at 660 cm^{-1}, 374 cm^{-1}, and 320 cm^{-1} indicates the formation of spinel Mn_3O_4. Upon examination of the high wavenumber region of Mn_2O_3 spectra, the formation of a low-intensity D peak forming between 1250 cm^{-1} and 1400 cm^{-1} indicates that the process caused minor defects to the underlying graphene. In the Mn_3O_4 spectra, this D peak formation did not occur, indicating this transformation did not defect the underlying graphene Additionally, the maintenance of the 2D FWHM between 50 and 70 cm^{-1} in both spectra indicates the bilayer character of the QEG is maintained through the annealing process.

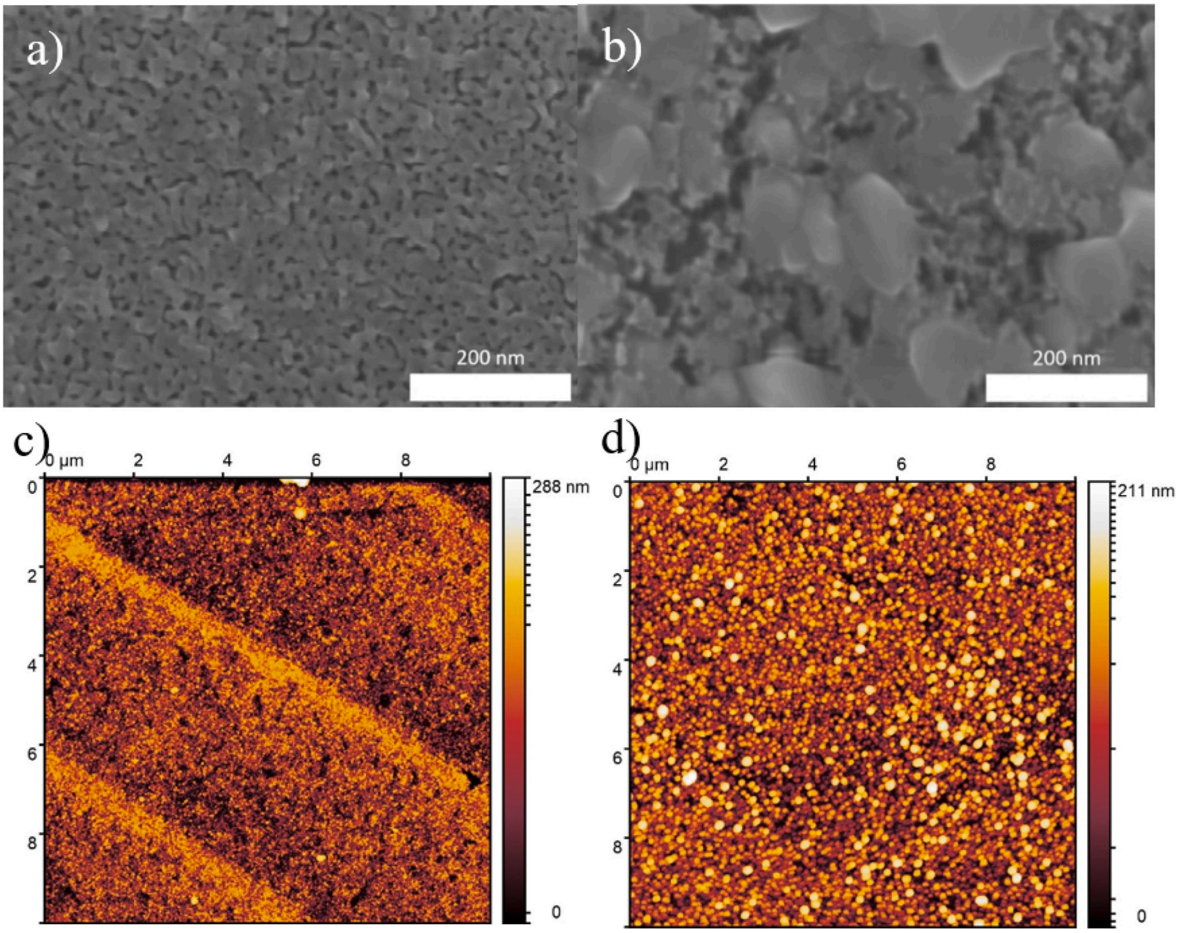

Fig. 10. SEM(a-b) taken at 80 Kx magnification and AFM (c–d) images of (a,c) Mn_2O_3, and (b,d)Mn_3O_4. The initial nanofibrous appearance of the δ-MnO_2 (Fig. 2) is transformed to a nonporous structure (b) after annealing in air, which is confirmed by the increased surface roughness in the AFM (c). After annealing in argon the δ-MnO_2 is transformed into large nanocubes connected by nanowalls (b), which is an unexpected morphology. In addition, the AFM for Mn_3O_4 no longer has clear features from the SiC step edges, which could be due to significant increases in the surface roughness.

also taken to confirm the change in surface morphology observed in the SEM images. These images indicated the transformation significantly increased the surface roughness, with values of 6.5 nm and 18.9 nm for Mn_2O_3 and Mn_3O_4, respectively, which is consistent with the surface morphology changes observed in the SEM (Fig. 10c-d). An approximately 30 % thickness reduction with the transformation from δ-MnO_2 to Mn_2O_3 was also observed. This observation is consistent with the transformation from the epitaxial layered δ-MnO_2 with a z-direction lattice constant of $c_{\delta-MnO_2} = 14.61$ Å to α-Mn_2O_3 with a z-direction lattice constant $a_{Mn_2O_3} = 9.41$ Å predicting a 35 % thickness reduction if the δ-MnO_2 is epitaxial and layered [6]. This thickness reduction was also observed after transformation to Mn_3O_4, which is similarly consistent with the expected reduction in the z-direction lattice constant from $c_{\delta-MnO_2} = 14.61$ Å to $a_{Mn_3O_4} = 9.81$ predicting a thickness reduction of 33 %. This further corroborates our previous conclusion that despite the nanofibrous surface of the film, it is generally epitaxial and planar, which is what we had desired.

5. Conclusion

δ-MnO_2/QEG heterostructures were synthesized and optimized to produce high-quality thin films of epitaxial δ-MnO_2 on QEG. This was done without damaging or oxidizing the underlying graphene, which has proven challenging in the literature and provides a good platform for further development in the areas of battery cathodes, with the additional benefit of not requiring toxic materials or precursors. The small potential barrier we discovered also indicates the heterostructure can be used in redox applications such as gas sensing, wherein it demonstrated the ability to be used as an intercalation-based gas sensor, discriminating based on molecular charge and size in preliminary testing. However additional testing is needed to fully characterize and understand these intercalation dynamics. These heterostructures were then annealed in air and Ar to form Mn_2O_3 and Mn_3O_4/QEG heterostructures, respectively. Analysis of the Raman spectra of these heterostructures indicated that the annealing process did not significantly defect or oxidize the underlying graphene substrate and that the resulting MnO_x materials were well crystallized. SEM images indicated that these heterostructures had nanostructured characteristics, including nanofibers, nanocubes, and nanopores, which would improve the reactive surface area of the resulting materials, which is desirable in oxygen reduction and oxygen evolution reactions, and energy storage applications. Additionally, due to these materials being formed on SiC, they are inherently compatible with traditional lithography capabilities, which further underlines their potential as a platform for next-generation electronics. This, combined with the high deposition speed, consistency, and potential scalability of the synthesis methods, makes this an exciting structure for additional research. However, significant questions remain. For the δ-MnO_2/QEG heterostructure, the effect of pattering on the potential device performance and the ability to transform from H-Type to X-Type birnessite is of significant interest. For the lower oxidation state MnO_x compounds, the formation of these materials on graphene was first demonstrated in this work. Therefore, the effect of this heterostructure on the underlying material requires more exploration to determine its potential applications.

Distribution statement A

Approved for public release. Distribution unlimited.

CRediT authorship contribution statement

Michael Pedowitz: Conceptualization, Formal analysis, Investigation, Validation, Writing – original draft, Writing – review & editing, Visualization. **Daniel Lewis:** Investigation. **Jennifer DeMell:** Investigation. **Daniel J. Pennachio:** Resources, Writing – review & editing. **Jenifer R. Hajzus:** Resources, Writing – review & editing. **Rachael Myers-Ward:** Resources, Writing – review & editing. **Soaram Kim:** Investigation, Supervision, Writing – review & editing. **Kevin M. Daniels:** Conceptualization, Funding acquisition, Project administration, Supervision, Writing – review & editing.

Declaration of competing interest

The authors declare that they have no known competing financial interests or personal relationships that could have appeared to influence the work reported in this paper.

Data availability

Data will be made available on request.

Acknowledgments

This work was supported by the NSF under the award CBET-2145549. Funding for the AFM shared facility used in this research was provided by the NSF under the award CHE-1626288. This research was performed while DJP held an NRC Research Associateship award at the U.S. Naval Research Laboratory. JRH acknowledges the American Society for Engineering Education Naval Research Laboratory Postdoctoral Fellow program. Work at the Naval Research Laboratory is supported by the Office of Naval Research.

Appendix A. Supplementary data

Supplementary data to this article can be found online at https://doi.org/10.1016/j.mtadv.2024.100467.

References

[1] K.S. Novoselov, et al., Electric Field effect in atomically thin carbon films, Science 306 (5696) (2004/10/22 2004) 666–669, https://doi.org/10.1126/science.1102896.

[2] Y.-L. Huang, C. Pellegrinelli, E.D. Wachsman, CO2 and O2 Co-exchange on multivalent metal oxides, J. Phys. Chem. C 123 (29) (2019/07/25 2019) 17711–17718, https://doi.org/10.1021/acs.jpcc.9b03774.

[3] Y. Liang, H. Dong, D. Aurbach, Y. Yao, Current status and future directions of multivalent metal-ion batteries, Nat. Energy 5 (9) (2020/09/01 2020) 646–656, https://doi.org/10.1038/s41560-020-0655-0.

[4] L. Spinelle, M. Gerboles, G. Kok, S. Persijn, T. Sauerwald, Review of portable and low-cost sensors for the ambient air monitoring of benzene and other volatile organic compounds, Sensors 17 (7) (2017), https://doi.org/10.3390/s17071520.

[5] H. Veeramani, et al., Low-temperature green synthesis of multivalent manganese oxide nanowires, ACS Sustain. Chem. Eng. 1 (9) (2013/09/03 2013) 1070–1074, https://doi.org/10.1021/sc400129n.

[6] C.M. Julien, M. Massot, C. Poinsignon, Lattice vibrations of manganese oxides: Part I. Periodic structures, Spectrochim. Acta Mol. Biomol. Spectrosc. 60 (3) (2004/02/01/2004) 689–700, https://doi.org/10.1016/S1386-1425(03)00279-8.

[7] Y. Liao, X. Zhang, R. Peng, M. Zhao, D. Ye, Catalytic properties of manganese oxide polyhedra with hollow and solid morphologies in toluene removal, Appl. Surf. Sci. 405 (2017/05/31/2017) 20–28, https://doi.org/10.1016/j.apsusc.2017.02.012.

[8] M.D. Pedowitz, et al., Fast selective sensing of nitrogen-based gases utilizing δ-MnO$_2$-epitaxial graphene-silicon carbide heterostructures for room temperature gas sensing, J. Microelectromech. Syst. 29 (5) (2020) 846–852, https://doi.org/10.1109/JMEMS.2020.3007342.

[9] C. Wu, et al., Electrochemically activated spinel manganese oxide for rechargeable aqueous aluminum battery, Nat. Commun. 10 (1) (2019/01/08 2019) 73, https://doi.org/10.1038/s41467-018-07980-7.

[10] D. Wang, et al., A superior δ-MnO2 cathode and a self-healing Zn-δ-MnO2 battery, ACS Nano 13 (9) (2019/09/24 2019) 10643–10652, https://doi.org/10.1021/acsnano.9b04916.

[11] W. Zhang, H. Jin, Y. Du, Y. Zhang, Z. Wang, J. Zhang, Hierarchical lamellar-structured MnO2@graphene for high performance Li, Na and K ion batteries, ChemistrySelect 40 (2020) 12481–12486, https://doi.org/10.1002/slct.202003584, 2020/10/29.

[12] T. Ozkaya, A. Baykal, H. Kavas, Y. Köseoğlu, M.S. Toprak, A novel synthetic route to Mn3O4 nanoparticles and their magnetic evaluation, Phys. B Condens. Matter 403 (19) (2008/10/01/2008) 3760–3764, https://doi.org/10.1016/j.physb.2008.07.002.

[13] V.P. Santos, S.A.C. Carabineiro, P.B. Tavares, M.F.R. Pereira, J.J.M. Órfão, J. L. Figueiredo, Oxidation of CO, ethanol and toluene over TiO2 supported noble metal catalysts, Appl. Catal. B Environ. 99 (1) (2010) 198–205, https://doi.org/10.1016/j.apcatb.2010.06.020. /08/31/2010.

[14] V.C. Bose, K. Maniammal, G. Madhu, C.L. Veenas, A.S.A. Raj, V. Biju, DC electrical conductivity of nanocrystalline Mn3O4 synthesized through a novel sol-gel route, IOP Conf. Ser. Mater. Sci. Eng. 73 (2015/02/17 2015) 012084, https://doi.org/10.1088/1757-899x/73/1/012084.

[15] F.K. Tan, J. Hassan, Z.A. Wahab, R.a.S. Azis, Electrical conductivity and dielectric behaviour of manganese and vanadium mixed oxide prepared by conventional solid state method, Engineering Science and Technology, an International Journal 19 (4) (2016/12/01/2016) 2081–2087, https://doi.org/10.1016/j.jestch.2016.08.002.

[16] Q. Zhang, et al., One-step hydrothermal synthesis of MnO2/graphene composite for electrochemical energy storage, J. Electroanal. Chem. 837 (2019/03/15/2019) 108–115, https://doi.org/10.1016/j.jelechem.2019.02.031.

[17] Y. Liu, et al., Manganese dioxide nanosheet arrays grown on graphene oxide as an advanced electrode material for supercapacitors, Electrochim. Acta 117 (2014/01/20/2014) 528–533, https://doi.org/10.1016/j.electacta.2013.11.121.

[18] L. Wang, W. Ma, Y. Li, H. Cui, "Synthesis of δ-MnO$_2$ with nanoflower-like architecture by a microwave-assisted hydrothermal method,", J. Sol. Gel Sci. Technol. 82 (1) (Apr 2017) 85–91, https://doi.org/10.1007/s10971-016-4275-x, 2021- 03-26 2017.

[19] B. Zhao, et al., Self-assembly of ultrathin MnO2/graphene with three-dimension hierarchical structure by ultrasonic-assisted co-precipitation method, J. Alloys Compd. 663 (2016/04/05/2016) 180–186, https://doi.org/10.1016/j.jallcom.2015.12.018.

[20] H. Han, Q.A. Sial, S.S. Kalanur, H. Seo, Binder assisted self-assembly of graphene oxide/Mn2O3 nanocomposite electrode on Ni foam for efficient supercapacitor application, Part A, Ceram. Int. 46 (10) (2020) 15631–15637, https://doi.org/10.1016/j.ceramint.2020.03.111, 2020/07/01/.

[21] Q. Li, Y. Li, A.V. Fulari, G.S. Ghodake, D.Y. Kim, G.M. Lohar, Performance of chemically synthesized Mn3O4/rGO nanocomposite for electrochemical supercapacitor: a cost-effective high-performance electrode, Nanotechnology 31 (41) (2020/07/21 2020) 415403, https://doi.org/10.1088/1361-6528/ab9f77.

[22] C. Gómez-Navarro, et al., Electronic transport properties of individual chemically reduced graphene oxide sheets, Nano Lett. 7 (11) (2007/11/01 2007) 3499–3503, https://doi.org/10.1021/nl072090c.

[23] K.M. Daniels, et al., Narrow plasmon resonances enabled by quasi-freestanding bilayer epitaxial graphene, 2D Mater. 4 (2) (2017/02/17 2017) 025034, https://doi.org/10.1088/2053-1583/aa5c75.

[24] S. Dhingra, J.-F. Hsu, I. Vlassiouk, B. D'Urso, Chemical vapor deposition of graphene on large-domain ultra-flat copper, Carbon 69 (2014/04/01/2014) 188–193, https://doi.org/10.1016/j.carbon.2013.12.014.

[25] M.G. Lawrence, The relationship between relative humidity and the dewpoint temperature in moist air: a simple conversion and applications, Bull. Am. Meteorol. Soc. 86 (2) (2005) 225–234, https://doi.org/10.1175/BAMS-86-2-225 (in English).

[26] K.M. Daniels, et al., Electrochemical hydrogenation of dimensional carbon, ECS Trans. 58 (4) (2013/08/31 2013) 439–445, https://doi.org/10.1149/05804.0439ecst.

[27] C. Zhu, et al., Self-branched α-MnO2/δ-MnO2 heterojunction nanowires with enhanced pseudocapacitance, Mater. Horiz. 4 (3) (2017) 415–422, https://doi.org/10.1039/C6MH00556J, 10.1039/C6MH00556J.

[28] C. Julien, M. Massot, R. Baddour-Hadjean, S. Franger, S. Bach, J.P. Pereira-Ramos, Raman spectra of birnessite manganese dioxides, Solid State Ionics 159 (3) (2003/04/01/2003) 345–356, https://doi.org/10.1016/S0167-2738(03)00035-3.

[29] D. Chen, et al., Probing the charge storage mechanism of a pseudocapacitive MnO2 electrode using in operando Raman spectroscopy, Chem. Mater. 27 (19) (2015/10/13 2015) 6608–6619, https://doi.org/10.1021/acs.chemmater.5b03118.

[30] T.-H. Wu, et al., Charge storage mechanism of activated manganese oxide composites for pseudocapacitors, J. Mater. Chem. A 10 (24) (2015) 12786–12795, https://doi.org/10.1039/C5TA03334A, 1039/C5TA03334A.

[31] T. Barudžija, N. Cvjetićanin, D. Bajuk-Bogdanović, M. Mojović, M. Mitrić, Vibrational and electron paramagnetic resonance spectroscopic studies of β-MnO2 and α-KxMnO2 nanorods, J. Alloys Compd. 728 (2017/12/25/2017) 259–270, https://doi.org/10.1016/j.jallcom.2017.09.015.

[32] S. Ma, X. Ye, X. Jiang, W. Cen, W. Jiang, H. Wang, First principles calculation of mechanical, dynamical and thermodynamic properties of MnO2 with four crystal phases, J. Alloys Compd. 852 (2021) 157007, https://doi.org/10.1016/j.jallcom.2020.157007, 2021/01/25/.

[33] K. Selvakumar, et al., Development of α-MnO2 nanowire with Ni- and (Ni, Co)-Cation doping as an efficient bifunctional oxygen evolution and oxygen reduction reaction catalyst, Chemelectrochem 9 (2) (2022) e202101303, https://doi.org/10.1002/celc.202101303, 2022/01/27.

[34] R. Ponnusamy, R. Venkatesan, M. Kandasamy, B. Chakraborty, C.S. Rout, MnO2 polymorph selection for non-enzymatic glucose detection: an integrated experimental and density functional theory investigation, Appl. Surf. Sci. 487 (2019/09/01/2019) 1033–1042, https://doi.org/10.1016/j.apsusc.2019.05.190.

[35] A.S. Poyraz, et al., Synthesis of cryptomelane type α-MnO2 (KxMn8O16) cathode materials with tunable K+ content: the role of tunnel cation concentration on electrochemistry, J. Mater. Chem. A 5 (32) (2017) 16914–16928, https://doi.org/10.1039/C7TA03476H, 10.1039/C7TA03476H.

[36] S.A. Alzahrani, S.A. Al-Thabaiti, W.S. Al-Arjan, M.A. Malik, Z. Khan, Preparation of ultra long α-MnO2 and Ag@MnO2 nanoparticles by seedless approach and their photocatalytic performance, J. Mol. Struct. 1137 (2017/06/05/2017) 495–505, https://doi.org/10.1016/j.molstruc.2017.02.068.

[37] C. Revathi, R.T.R. Kumar, Electro catalytic properties of α, β, γ, ϵ - MnO2 and γ - MnOOH nanoparticles: role of polymorphs on enzyme free H2O2 sensing, Electroanalysis 29 (5) (2017/05/01 2017) 1481–1489, https://doi.org/10.1002/elan.201600608.

[38] T. Gao, H. Fjellvåg, P. Norby, A comparison study on Raman scattering properties of α- and β-MnO2, Anal. Chim. Acta 648 (2) (2009/08/26/2009) 235–239, https://doi.org/10.1016/j.aca.2009.06.059.

[39] T. Lin, L. Yu, M. Sun, G. Cheng, B. Lan, Z. Fu, Mesoporous α-MnO2 microspheres with high specific surface area: controlled synthesis and catalytic activities, Chem. Eng. J. 286 (2016/02/15/2016) 114–121, https://doi.org/10.1016/j.cej.2015.09.024.

[40] L. Yan, et al., Experimental and theoretical investigation of the effect of oxygen vacancies on the electronic structure and pseudocapacitance of MnO2, ChemSusChem 12 (15) (2019/08/08 2019) 3571–3581, https://doi.org/10.1002/cssc.201901015.

[41] V.A. Drits, E. Silvester, A.I. Gorshkov, A. Manceau, Structure of synthetic monoclinic Na-rich birnessite and hexagonal birnessite: I. Results from X-ray diffraction and selected-area electron diffraction, Am. Mineral. 82 (9-10) (1997) 946–961.

[42] D. Li, W. Li, Y. Deng, X. Wu, N. Han, Y. Chen, Effective Ti doping of δ-MnO2 via anion route for highly active catalytic combustion of benzene, J. Phys. Chem. C 120 (19) (2016/05/19 2016) 10275–10282, https://doi.org/10.1021/acs.jpcc.6b00931.

[43] Z.M. Chan, et al., Electrochemical trapping of metastable Mn^{3+} ions for activation of MnO_2 oxygen evolution catalysts, Proc. Natl. Acad. Sci. USA 115 (23) (2018) E5261–E5268, https://doi.org/10.1073/pnas.1722235115.

[44] L. Yang, S. Cheng, X. Ji, Y. Jiang, J. Zhou, M. Liu, Investigations into the origin of pseudocapacitive behavior of Mn3O4 electrodes using in operando Raman spectroscopy, J. Mater. Chem. A 10 (14) (2015) 7338–7344, https://doi.org/10.1039/C5TA00223K, 1039/C5TA00223K.

[45] S. Lin, Z. Chen, L. Li, C. Yang, Effect of impurities on the Raman scattering of 6H-SiC crystals, Mater. Res. 15 (2012) 833–836.

[46] V.R. Galakhov, et al., Mn $3s$ exchange splitting in mixed-valence manganites, Phys. Rev. B 65 (11) (2002) 113102, https://doi.org/10.1103/PhysRevB.65.113102.

[47] A. Bauer, et al., High-precision determination of atomic positions in crystals: the case of $6H$- and $4H$-SiC, Phys. Rev. B 57 (5) (1998) 2647–2650, https://doi.org/10.1103/PhysRevB.57.2647.

[48] R.K. Sharma, A.C. Rastogi, S.B. Desu, Manganese oxide embedded polypyrrole nanocomposites for electrochemical supercapacitor, Electrochim. Acta 53 (26) (2008/11/01/2008) 7690–7695, https://doi.org/10.1016/j.electacta.2008.04.028.

[49] Y. Huang, et al., Universal mechanical exfoliation of large-area 2D crystals, Nat. Commun. 11 (1) (2020/05/15 2020) 2453, https://doi.org/10.1038/s41467-020-16266-w.

[50] W. Melitz, J. Shen, A.C. Kummel, S. Lee, Kelvin probe force microscopy and its application, Surf. Sci. Rep. 66 (1) (2011/01/01/2011) 1–27, https://doi.org/10.1016/j.surfrep.2010.10.001.

[51] S. Mammadov, et al., Work function of graphene multilayers on SiC(0001), 2D Mater. 4 (1) (2017/01/16 2017) 015043, https://doi.org/10.1088/2053-1583/4/1/015043.

[52] N. Joshi, T. Hayasaka, Y. Liu, H. Liu, O.N. Oliveira, L. Lin, A review on chemiresistive room temperature gas sensors based on metal oxide nanostructures, graphene and 2D transition metal dichalcogenides, Microchim. Acta 185 (4) (2018/03/10 2018) 213, https://doi.org/10.1007/s00604-018-2750-5.

[53] G. Jung, et al., Comparison of the characteristics of semiconductor gas sensors with different transducers fabricated on the same substrate, Sensor. Actuator. B Chem. 335 (2021/05/15/2021) 129661, https://doi.org/10.1016/j.snb.2021.129661.

[54] D. Gu, et al., Visible-light activated room temperature NO2 sensing of SnS2 nanosheets based chemiresistive sensors, Sensor. Actuator. B Chem. 305 (2020/02/15/2020) 127455, https://doi.org/10.1016/j.snb.2019.127455.

[55] T. Alkathiri, et al., 2D palladium sulphate for visible-light-driven optoelectronic reversible gas sensing at room temperature, Small Science 2 (3) (2022/03/01 2022) 2100097, https://doi.org/10.1002/smsc.202100097.

[56] I.V. Leontyev, A.A. Stuchebrukhov, Electronic polarizability and the effective pair potentials of water, J. Chem. Theor. Comput. 6 (10) (2010/10/12 2010) 3153–3161, https://doi.org/10.1021/ct1002048.

[57] X. Gu, J. Yue, L. Li, H. Xue, J. Yang, X. Zhao, General synthesis of MnOx (MnO2, Mn2O3, Mn3O4, MnO) hierarchical microspheres as lithium-ion battery anodes, Electrochim. Acta 184 (2015/12/01/2015) 250–256, https://doi.org/10.1016/j.electacta.2015.10.037.

[58] M.H. Oliveira, et al., Formation of high-quality quasi-free-standing bilayer graphene on SiC(0001) by oxygen intercalation upon annealing in air, Carbon 52 (2013/02/01/2013) 83–89, https://doi.org/10.1016/j.carbon.2012.09.008.

[59] S.H. Shim, D. LaBounty, T.S. Duffy, Raman spectra of bixbyite, Mn2O3, up to 40 GPa, Phys. Chem. Miner. 38 (9) (2011/06/12 2011) 685, https://doi.org/10.1007/s00269-011-0441-4.